

Single Pion Production off Free Nucleons: Analysis of Photon, Electron, Pion and Neutrino Induced Processes

M. Kabirnezhad

*Imperial College London, Department of Physics, London SW7 2BZ, United Kingdom **

(Dated: September 5, 2024)

In this paper, I introduce a unified model for single-pion production across photo-, electro-, and neutrino-nucleon interactions, designed to be valid over a broad kinematic range that is crucial for accelerator-based neutrino experiments. This model includes vector and axial-vector nucleon transition form factors for all excited nucleons or resonances up to 2 GeV, as well as non-resonant backgrounds, within a meson dominance framework that adheres to QCD principles and ensures unitarity. This approach guarantees accurate asymptotic behaviour at high momentum transfer (Q^2) and effectively addresses the transition region. Additionally, the model employs the Conserved Vector Current (CVC) and Partially Conserved Axial Current (PCAC) relations to provide reliable predictions at very low Q^2 , tackling challenges encountered by current neutrino experiments.

The unified model facilitates a comprehensive analysis by integrating all available data from electron, photon, pion, and neutrino scattering experiments. This integration enables a detailed investigation of nucleon structure within the resonance region and is particularly valuable for probing weak interactions, where neutrino-nucleon data are limited. The combined analysis allows for the simultaneous parameterisation and constraint of the model's free parameters, while quantifying associated uncertainties, thus providing a robust and reliable framework for future neutrino measurements.

I. INTRODUCTION

Neutrino interactions that result in the production of a single pion in the final state are critically important for accelerator-based neutrino experiments. Single pion production (SPP) channels constitute the largest fraction of the inclusive neutrino-nucleus cross-section in the 1 – 5 GeV energy region, which is relevant for all accelerator-based neutrino beams. Accurate models of SPP cross-section processes are required to precisely predict the number and kinematics of neutrino interactions. These models help establish the relationship between neutrino energy and energy deposition in a neutrino detector, which is crucial for interpreting experimental results and reducing systematic uncertainties. Therefore, it is essential that these models are valid within the kinematic region of the neutrino experiments.

Chiral perturbation theory (ChPT), the effective field theory of QCD, is adept at describing non-perturbative QCD processes, such as pion production, particularly at neutrino energies around 1 GeV. This makes ChPT highly useful for understanding interactions in this energy range. However, current and future neutrino experiments, such as NOvA and DUNE, operate in a wide energy beam that includes higher energies. These experiments explore a transition region where neutrino energies exceed $E_\nu = 1$ GeV but remain below the energies where perturbative QCD becomes the dominant framework. This kinematic region, spanning both perturbative and non-perturbative regimes, features hadronic degrees of freedom that are a mixture of nucleons, resonances, and partons. This presents unique challenges in

accurately modelling the interactions and particle productions observed in these experiments. This can explain current discrepancies in the first resonance region between MiniBooNE and MINERvA experiments, which have been discussed in Ref. [12].

Additionally, the transition region encompasses several processes where both resonant and non-resonant mechanisms play a role. Currently, 18 overlapping resonances with varying quantum numbers have been identified, each with resonance masses below 2 GeV. These overlapping resonances result in significant interference effects, not only among the resonances themselves but also between resonant and non-resonant interactions. Such complex interference patterns add to the difficulty of accurately understanding pion production. Therefore, a thorough understanding of these processes within the transition region is crucial for improving the precision of neutrino interaction predictions. Figure 1 illustrates these complexities: the left panel shows how the hadron invariant mass W evolves, while the right panel depicts the corresponding Q^2 evolution, mapping out the regions explored by both current and future neutrino experiments.

In addition to model development and robust predictions, a crucial aspect of theoretical work in neutrino experiments is the quantification of uncertainties. While several SPP models exist, most of them address only key processes, focusing primarily on the first and second resonance regions. However, none of these models systematically study or evaluate the systematic uncertainties inherent to the models themselves. Furthermore, existing SPP models are confined to the non-perturbative region, which does not encompass the broad kinematic range required for neutrino experiments. The primary goal of this work is to develop a comprehensive model that addresses these gaps, providing a robust framework to enhance the

* m.kabirnezhad@imperial.ac.uk

precision of neutrino measurements.

The valid region for the SPP model presented in this paper is defined by a hadron invariant mass (W) below 2 GeV, as illustrated in Fig. 1. This region is characterised by broad nucleon excitations superimposed on a smooth non-resonant background. For hadron invariant masses below 1.4 GeV, the target nucleon is predominantly excited to the $\Delta(1232)$ resonance, which then decays almost immediately into a single pion and a nucleon. In this lower mass range, the Δ resonance, with its significant contribution, is the sole resonance observed within the first resonance region ($1.08\text{GeV} < W < 1.4\text{ GeV}$).

The dynamics of the interactions become more intricate in the second resonance region ($1.4\text{ GeV} < W < 1.6\text{GeV}$), where the scattering processes are influenced by three isospin-1/2 resonances: the $P_{11}(1440)$ Roper resonance, and two negative-parity states, $D_{13}(1520)$ and $S_{11}(1535)$. As W continues to rise into the third resonance region ($1.6\text{GeV} < W < 2.0\text{ GeV}$), the complexity further escalates with the contribution of an additional ten four-star resonances, as noted in Ref. [9], significantly enriching the interaction dynamics.

A commonly used form factor in theoretical models, derived from elastic electron scattering data, is the dipole form factor. However, inelastic scattering data indicate that the dipole form factor is inadequate for accurately describing excited nucleons, particularly in the transition region. In contrast, the meson dominance (MD) form factor model, which accounts for the interaction between leptons and nucleons via meson exchange with analogous quantum properties, offers a more accurate representation. As emphasised in Ref. [13], the MD model, consistent with QCD calculations, effectively captures the nucleon form factor across both perturbative and non-perturbative regimes, particularly addressing the hadron-quark transition region. The model incorporates several parameters that can be constrained by unitarity conditions and analytic models. However, precise quantification of these form factors requires accurate data across a broad kinematic range—a challenge compounded by the scarcity of available data for neutrino interactions in this context.

To address this challenge, this paper introduces a comprehensive unified model that extends its applicability to analogous processes involving not only neutrino beams but also electron, photon, and pion beams. The integration of these diverse probes is particularly advantageous, as electron, photon, and pion scattering experiments have yielded a wealth of data over the years, covering a broad range of kinematic conditions. By harnessing this extensive dataset, the model enables a more detailed and nuanced investigation of nucleon structure, offering insights that would be difficult to achieve using neutrino data alone.

The unified model capitalises on the strengths of each interaction type: electron scattering data provides precision and control for probing the vector current, photon interactions offer complementary insights into the vector

current at very low Q^2 , and pion scattering data, guided by the Partially Conserved Axial Current (PCAC) hypothesis, delivers crucial information on the axial-vector current at low Q^2 . This comprehensive dataset is particularly valuable for addressing and potentially resolving discrepancies between single-pion production (SPP) models and neutrino data, especially in the low Q^2 region ($Q^2 < 0.2, \text{GeV}^2$).

The advanced theoretical framework developed in this work is designed to incorporate these diverse datasets seamlessly, ensuring that the model remains consistent with fundamental QCD principles and preserves all symmetry relations. This consistency is crucial for making robust predictions about nucleon behaviour across various experimental contexts. Furthermore, the sophisticated analysis method employed in this paper allows for meticulous control over systematic uncertainties, which primarily arise from experimental data and the choice of model parametrisation. Robust predictions with quantified uncertainties are essential for precision neutrino measurements, paving the way for future discoveries.

II. MK MODEL (GENERAL DESCRIPTION)

Let us consider the weak, electro- and photo- pion production reactions:

$$\begin{aligned} \left. \begin{matrix} \nu_l \\ \bar{\nu}_l \end{matrix} \right\} (k_1) + N(p_1) &\rightarrow \left. \begin{matrix} l \\ \bar{l} \end{matrix} \right\} (k_2) + N(p_2) + \pi(q), \\ e(k_1) + N(p_1) &\rightarrow e(k_2) + N(p_2) + \pi(q), \\ \gamma(k) + N(p_1) &\rightarrow N(p_2) + \pi(q) \end{aligned} \quad (1)$$

Here N represents a nucleon and l denotes the outgoing charged lepton or neutrino in charged current (CC) and neutral current (NC) interactions. The four-momentum of each particle is indicated in parentheses. In the weak and electro-production reactions, the momentum transfer is defined by $\mathbf{k} = \mathbf{k}_1 - \mathbf{k}_2$, and the invariant quantities Q^2 and W are given by:

$$\begin{aligned} Q^2 &= -k^2 = -(k_1 - k_2)^2, \\ W^2 &= (k + p_1)^2 = (p_2 + q)^2. \end{aligned}$$

Non-invariant quantities, such as pion angles, are defined in the centre-of-mass frame of the final pion and nucleon (the isobaric frame). This is represented by the equation:

$$\mathbf{q} + \mathbf{p}_2 = \mathbf{k} + \mathbf{p}_1 = 0. \quad (2)$$

The pion angles in the isobaric frame are illustrated in Fig. 2. Variables in the laboratory frame are labeled by L . In this framework, the full kinematic differential cross section for single pion production in lepton-nucleon scattering is defined as:

$$\frac{d\sigma(lN \rightarrow l'N\pi)}{dk^2 dW d\Omega_\pi} = \frac{1}{(2\pi)^4} \frac{|\mathbf{q}|}{8M^2} \frac{-k^2}{(\mathbf{k}^L)^2} |\mathcal{M}|^2 \quad (3)$$

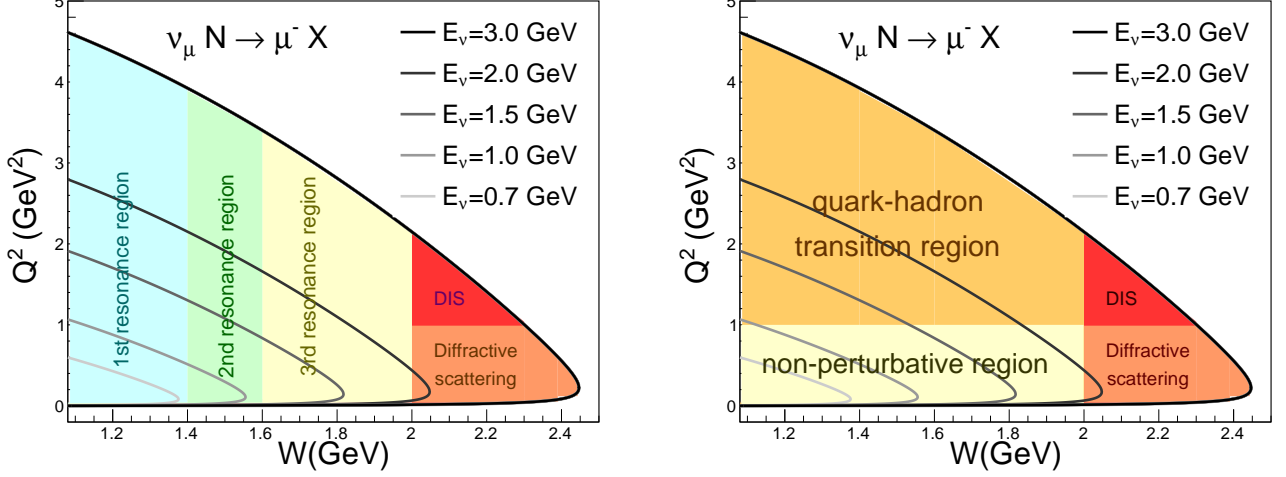


FIG. 1. The allowed kinematic region for a charge-current inelastic neutrino-nucleon interaction in terms of Q^2 and W for different neutrino energy. The left plot shows the W evolution and different resonance regions. The right plot shows the Q^2 evolution and the quark-hadron transition. The phase space for $E_\nu < 2$ GeV doesn't go beyond the resonance region.

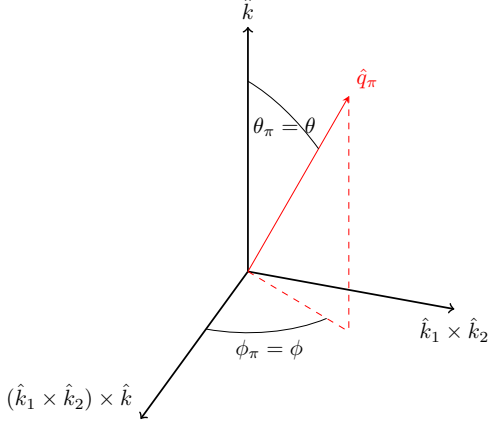


FIG. 2. Isobaric frame or the πN center-of-mass frame.

where \mathcal{M} , the matrix element for weak and electromagnetic interactions, can be expressed as follows:

$$\begin{aligned}
 \mathcal{M}(\nu_l N \rightarrow l N \pi) &= \frac{G_F}{\sqrt{2}} a \epsilon_\rho \langle N \pi | J_{CC+}^\rho | N \rangle \\
 \mathcal{M}(\bar{\nu}_l N \rightarrow \bar{l} N \pi) &= \frac{G_F}{\sqrt{2}} a \bar{\epsilon}_\rho \langle N \pi | J_{CC-}^\rho | N \rangle \\
 \mathcal{M}(e N \rightarrow e' N \pi) &= e^2 \epsilon_\rho^{EM} \frac{1}{k^2} \langle N \pi | J_{EM}^\rho | N \rangle
 \end{aligned} \tag{4}$$

where G_F is the Fermi coupling constant, and e is the electric charge. ϵ^ρ is the leptonic current and a is either the cosine of the Cabibbo angle for CC interactions or $\frac{1}{2}$

for NC interactions.

$$\begin{aligned}
 \epsilon_\rho &= \bar{u}_l(k_2) \gamma_\rho (1 - \gamma_5) u_\nu(k_1), \\
 \bar{\epsilon}_\rho &= \bar{u}_{\bar{l}}(k_2) \gamma_\rho (1 + \gamma_5) u_{\bar{\nu}}(k_1), \\
 \epsilon_\rho^{EM} &= \bar{u}_e(k_2) \gamma^\rho u_e(k_1),
 \end{aligned} \tag{5}$$

where u is the spinor of leptons. The lepton current (ϵ^ρ) can be interpreted as the intermediate gauge boson's polarisation vector:

$$\epsilon_\lambda^\rho = [C_{L_\lambda} e_L^\rho + C_{R_\lambda} e_R^\rho + C_\lambda e_\lambda^\rho], \tag{6}$$

where \mathbf{e}_L and \mathbf{e}_R are the transverse polarisations (i.e., perpendicular to the momentum transfer), and \mathbf{e}_λ is the longitudinal polarisation along the \mathbf{z} direction of the isobaric system. This gives:

$$\begin{aligned}
 e_L^\alpha &= \frac{1}{\sqrt{2}} (0 \ 1 \ -i \ 0), \\
 e_R^\alpha &= \frac{1}{\sqrt{2}} (0 \ -1 \ -i \ 0), \\
 e_\lambda^\alpha &= \frac{1}{\sqrt{[(\epsilon_\lambda^0)^2 - (\epsilon_\lambda^3)^2]}} (\epsilon_\lambda^0 \ 0 \ 0 \ \epsilon_\lambda^3)
 \end{aligned} \tag{7}$$

and,

$$\begin{aligned}
 C_{L_\lambda} &= \frac{1}{\sqrt{2}} (\epsilon_\lambda^1 + i \epsilon_\lambda^2), \\
 C_{R_\lambda} &= -\frac{1}{\sqrt{2}} (\epsilon_\lambda^1 - i \epsilon_\lambda^2), \\
 C_\lambda &= \sqrt{[(\epsilon_\lambda^0)^2 - (\epsilon_\lambda^3)^2]}.
 \end{aligned} \tag{8}$$

where $\lambda = -(+)$ stands for the left (right)-handed helicity. In NC weak current and electron scattering

lepton current, where the lepton mass is neglected, $\epsilon_+^\rho = 0$, therefore the gauge boson can be interpreted by three polarisations.

The electromagnetic hadron current is given by

$$J_{EM}^\rho = \frac{1}{2}\mathcal{V}_Y^\rho + \mathcal{V}_3^\rho. \quad (9)$$

The weak hadron currents can be decomposed into vector current(\mathcal{V}):

$$\begin{aligned} \mathcal{V}_{CC}^\rho &= \mathcal{V}_1^\rho + i\mathcal{V}_2^\rho, \\ \mathcal{V}_{NC}^\rho &= (1 - 2\sin\theta_W^2)\mathcal{V}_3^\rho - \sin\theta_W^2\mathcal{V}_Y^\rho - \frac{1}{2}\mathcal{V}_S^\rho, \end{aligned} \quad (10)$$

and axial-vector (\mathcal{A}):

$$\begin{aligned} \mathcal{A}_{CC}^\rho &= \mathcal{A}_1^\rho + i\mathcal{A}_2^\rho \\ \mathcal{A}_{NC}^\rho &= \mathcal{A}_3^\rho - \frac{1}{2}\mathcal{A}_S^\rho \end{aligned} \quad (11)$$

where $\mathcal{V}_{1,2,3}$ ($\mathcal{A}_{1,2,3}$) are the component of the isovector part of the vector (axial-vector) current, \mathcal{V}_Y and \mathcal{V}_S (\mathcal{A}_S) are hypercharge and strange isoscalar current.

Isospin symmetry establishes a connection between the matrix elements of the isovector components of the vector and axial-vector hadronic currents. Consequently, the matrix elements for antineutrino- and neutrino-induced reactions are proportional, given by:

$$\begin{aligned} \langle p\pi^- | J_\rho^{CC-} | p \rangle &= \langle n\pi^+ | J_\rho^{CC+} | n \rangle \\ \langle n\pi^- | J_\rho^{CC-} | n \rangle &= \langle p\pi^+ | J_\rho^{CC+} | p \rangle \\ \langle n\pi^0 | J_\rho^{CC-} | p \rangle &= -\langle p\pi^0 | J_\rho^{CC+} | n \rangle \end{aligned} \quad (12)$$

A real photon has two transverse polarisations.

The matrix elements in Eq. 4 can be written in terms of helicity amplitudes and the lepton coefficients in Eq. 8. The helicity amplitudes of the hadron current are defined with three indices: the helicity of the incident nucleon (λ_1), the helicity of the outgoing nucleon (λ_2), and the polarisation of the gauge boson (λ_k):

$$\begin{aligned} \tilde{F}_{\lambda_2, \lambda_1}^{\lambda_k} &= \langle N\pi | e_{\lambda_k}^\rho \left(\frac{1}{2W}\right) J_\rho^V | N \rangle, \\ \tilde{G}_{\lambda_2, \lambda_1}^{\lambda_k} &= \langle N\pi | e_{\lambda_k}^\rho \left(\frac{1}{2W}\right) J_\rho^A | N \rangle, \end{aligned} \quad (13)$$

Therefore, there are 16 helicity amplitudes to describe the vector current and 16 helicity amplitudes to describe the axial-vector current for weak CC interactions. For electron scattering and NC channels, the gauge boson has three polarisations; therefore, there are 12 helicity amplitudes for the electromagnetic current. For photon scattering, there are two polarisations and thus 8 helicity amplitudes.

The hadronic currents and helicity amplitudes involve several form factors. The most sophisticated model to describe these form factors is the meson dominance (MD)

TABLE I. (axial-) vector meson masses

k	ρ -group	$m_{(\rho)k}$ [GeV]	ω -group	$m_{(\omega)k}$ [GeV]
1	$\rho(770)$	0.77526	$\omega(782)$	0.78265
2	$\rho(1450)$	1.465	$\omega(1420)$	1.410
3	$\rho(1700)$	1.720	$\omega(1650)$	1.670
4	$\rho(1900)$	1.885	$\omega(1960)$	1.960
5	$\rho(2150)$	2.150	$\omega(2205)$	2.205
k	a_1 -group	$m_{(a_1)k}$ [GeV]	f_1 -group	$m_{(f_1)k}$ [GeV]
1	$a_1(1260)$	1.230	$f_1(1285)$	1.2819
2	$a_1(1420)$	1.411	$f_1(1420)$	1.4263
3	$a_1(1640)$	1.655	$f_1(1510)$	1.518
4	$a_1(2095)$	2.096	$f_1(1970)$	1.1971

model, based on the effective Lagrangian of quantum field theory as introduced by Sakurai and Gell-Mann in Refs. [4, 11]. The MD model explains the interaction between leptons and nucleons through meson exchange with analogous quantum properties. The form factors can then be expressed in terms of the meson masses (m_j), the ratio of coupling strengths between the gauge boson and the meson, and between the meson and the nucleon (a_j), summing over all possible n mesons:

$$FF_N(k^2) = \sum_{j=1}^n \frac{a_j m_j^2}{m_j^2 - k^2} \quad (14)$$

where a list of vector-mesons and axial-mesons is given in Table I.

There are two shortcomings from the form factor model; firstly, the FF_N in eq: 14 does not have analytic properties and does not obey the unitarity condition. secondly, the asymptotic behaviour of the form factor differs from the asymptotic scaling behaviours predicted by QCD. However these properties can be imposed to the MD model.

Imposing the conditions bring us to a complex system of equations for the coupling constant ratios, making it difficult to find solutions in the general case. However, in Ref. [1], an equivalent system of equations is derived for the coupling constant ratios, with coefficients that are simply even powers of the corresponding vector-meson masses. In principle, one can find solutions to these equations even in the general case, referred to as linear super-

convergence relations:

$$\begin{aligned}
\sum_{j=1}^n m_j^2 a_j &= 0, \\
\sum_{j=1}^n m_j^4 a_j &= 0, \\
&\vdots \\
\sum_{j=1}^n m_j^{2(m-1)} a_j &= 0,
\end{aligned} \tag{15}$$

where $m \leq n$ shows the asymptotic behaviour of the form factors:

$$FF_N(k^2)|_{|k^2| \rightarrow \infty} \sim k^{-2m}$$

III. RESONANCE PRODUCTION

The general form of helicity amplitudes was calculated in my previous papers [5–7], and these are reproduced in Appendix A and B. The 16 vector helicity amplitudes ($\tilde{F}_{\lambda_2, \lambda_1}^{\lambda_k}$) are presented in Table VI, and the 16 axial-vector helicity amplitudes ($\tilde{G}_{\lambda_2, \lambda_1}^{\lambda_k}$) are shown in Table VII. The definitions include several factors, such as Clebsch-Gordan coefficients for different SPP channels, branching ratios for each resonance decaying into a single pion, and Breit-Wigner parametrisation for the broad resonance states. These factors are common across all models. However, the key part of the definition lies in the resonance production amplitudes, which depend on the specific model chosen. The production amplitudes are calculated from the Feynman diagrams shown in Fig. 3. The goal of this section is to calculate these amplitudes, which are defined as follows:

$$\begin{aligned}
f_{-3}^{(V,A)} &= -\frac{1}{2W} \langle R, 3/2 | e_R^\rho J_\rho^{(V,A)} | N, 1/2 \rangle \\
f_{-1}^{(V,A)} &= -\frac{1}{2W} \langle R, 1/2 | e_R^\rho J_\rho^{(V,A)} | N, -1/2 \rangle \\
f_{0+}^{(V,A)(\lambda)} &= \frac{1}{2W} \frac{\sqrt{-k^2}}{|\mathbf{k}|} \langle R, 1/2 | e_R^\rho J_\rho^{(V,A)} | N, 1/2 \rangle
\end{aligned} \tag{16}$$

Here $f^{(V,A)}$ denotes the vector and axial-vector production amplitudes and $J^{(V,A)}$ represent hadron currents.

A. The first and second resonance regions

In the first and second resonance regions, the produced resonances correspond to the first four states listed in Table III. These resonances have spins of either 1/2 or 3/2.

FIG. 3. Resonance production in lepton scattering.

The hadronic currents associated with these resonances can be expressed as follows:

$$\begin{aligned}
\langle R(p) | J_{3/2}^\rho | N(p_1) \rangle &= \bar{\psi}_\alpha(p) \Gamma_{3/2}^{\alpha\rho} u(p_1, s_z) \\
\langle R(p) | J_{1/2}^\rho | N(p_1) \rangle &= \bar{u}(p) \Gamma_{1/2}^\rho u(p_1, s_z).
\end{aligned} \tag{17}$$

In these equations, $u(p)$ represents the Dirac spinor for spin-1/2 resonances, while $\psi_\alpha(p)$ denotes the Rarita-Schwinger spinor for spin-3/2 resonances. The operators $\Gamma_{3/2}^{\alpha\rho}$ and $\Gamma_{1/2}^\rho$ encapsulate the interaction dynamics and depend on the specific form of the current J^ρ , as well as the quantum numbers of the resonances involved. Given that the dynamics governing resonances with spin 1/2 and 3/2 differ significantly, I will discuss these cases separately to provide a clear understanding of their respective contributions:

1. Resonances with spin 3/2

In the first and second resonance regions, there are two resonances with spin 3/2: the P_{33} (Δ) resonance, which has positive parity, and the $D_{13}(1520)$ resonance, which has negative parity. Their corresponding interactions are defined as follows:

$$\begin{aligned}
\Gamma_{3/2}^{\alpha\rho}(P_{33}) &= [\mathcal{V}_{3/2}^{\alpha\rho} - \mathcal{A}_{3/2}^{\alpha\rho}] \gamma^5 \\
\Gamma_{3/2}^{\alpha\rho}(D_{13}) &= [\mathcal{V}_{3/2}^{\alpha\rho} - \mathcal{A}_{3/2}^{\alpha\rho}]
\end{aligned} \tag{18}$$

where the vector ($\mathcal{V}_{3/2}^{\alpha\rho}$) and axial-vector ($\mathcal{A}_{3/2}^{\alpha\rho}$) components are given by:

$$\begin{aligned}
\mathcal{V}_{3/2}^{\alpha\rho} &= \frac{\mathcal{C}_3^V}{M} (g^{\alpha\rho} \not{k} - k^\alpha \gamma^\rho) + \frac{\mathcal{C}_4^V}{M^2} (g^{\alpha\rho} k \cdot p - k^\alpha p^\rho) \\
&\quad + \frac{\mathcal{C}_5^V}{M^2} (g^{\alpha\rho} k \cdot p_1 - k^\alpha p_1^\rho), \\
\mathcal{A}_{3/2}^{\alpha\rho} &= \frac{\mathcal{C}_3^A}{M} (g^{\alpha\rho} \not{k} - k^\alpha \gamma^\rho) + \frac{\mathcal{C}_4^A}{M^2} (g^{\alpha\rho} k \cdot p - k^\alpha p^\rho) \\
&\quad + \mathcal{C}_5^A g^{\alpha\rho} + \frac{\mathcal{C}_6^A}{M^2} k^\alpha k^\rho.
\end{aligned} \tag{19}$$

The vector and axial-vector helicity amplitudes for the P_{33} and D_{13} resonances can be derived from Eqs. 16 and 19. Here, we present the explicit forms of these amplitudes for P_{33} resonance:

$$\begin{aligned}
f_{-3}^V(P_{33}) &= -\frac{|\mathbf{k}|}{W} \frac{1}{\sqrt{2\mathcal{N}}} \left[\frac{C_3^V W_+}{M} + \frac{C_4^V}{M^2} W k_0 + \frac{C_5^V}{M^2} (W k_0 - k^2) \right], \\
f_{-1}^V(P_{33}) &= \frac{|\mathbf{k}|}{W} \frac{1}{\sqrt{2\mathcal{N}}} \left[\frac{C_3^V}{MW} (k^2 - MW_+) + \frac{C_4^V}{M^2} W k_0 + \frac{C_5^V}{M^2} (W k_0 - k^2) \right], \\
f_{0+}^{V(\lambda)}(P_{33}) &= -\frac{|\mathbf{k}|}{W} \frac{1}{\sqrt{2\mathcal{N}}} \frac{1}{C_\lambda} (|\mathbf{k}| \epsilon_\lambda^0 - k_0 \epsilon_\lambda^z) \left[\frac{C_3^V}{M} + \frac{C_4^V}{M^2} W + \frac{C_5^V}{M^2} (W - k_0) \right]
\end{aligned} \tag{20}$$

$$\begin{aligned}
f_{-3}^A(P_{33}) &= -\sqrt{\frac{\mathcal{N}}{2}} \left[\frac{C_3^A W_-}{M} + \frac{C_4^A}{M^2} W k_0 + C_5^A \right], \\
f_{-1}^A(P_{33}) &= -\sqrt{\frac{\mathcal{N}}{6}} \left[\frac{C_3^A}{M} \frac{2|\mathbf{k}| + k_0 W_-}{E_k + M} - \frac{C_4^A}{M^2} W k_0 - C_5^A \right], \\
f_{0+}^{A(\lambda)}(P_{33}) &= -\sqrt{\frac{\mathcal{N}}{3}} \frac{1}{C_\lambda} \left[\left(\frac{C_3^A}{M} + \frac{C_4^A}{M^2} W \right) (|\mathbf{k}| \epsilon_\lambda^0 - k_0 \epsilon_\lambda^z) - C_5^A \epsilon^z + \frac{C_6^A}{M^2} |\mathbf{k}| (|\mathbf{k}| \epsilon_\lambda^0 - k_0 \epsilon_\lambda^z) \right]
\end{aligned} \tag{21}$$

and for D_{13} resonance:

$$\begin{aligned}
f_{-3}^V(D_{13}) &= \sqrt{\frac{\mathcal{N}}{2}} \left[\frac{C_3^V}{M} W_- + \frac{C_4^V}{M^2} W k_0 + \frac{C_5^V}{M^2} (W k_0 - k^2) \right], \\
f_{-1}^V(D_{13}) &= \sqrt{\frac{\mathcal{N}}{6}} \left[\frac{C_3^V}{M} \left(W_- - 2 \frac{\mathbf{k}^2}{E_k + M} \right) + \frac{C_4^V}{M^2} W k_0 + \frac{C_5^V}{M^2} (W k_0 - k^2) \right], \\
f_{0+}^{V(\lambda)}(D_{13}) &= \sqrt{\frac{\mathcal{N}}{3}} \frac{1}{C_\lambda} (|\mathbf{k}| \epsilon_\lambda^0 - k_0 \epsilon_\lambda^z) \left[\frac{C_3^V}{M} + \frac{C_4^V}{M^2} W + \frac{C_5^V}{M^2} (W - k_0) \right]
\end{aligned} \tag{22}$$

$$\begin{aligned}
f_{-3}^A(D_{13}) &= -\frac{|\mathbf{k}|}{W} \frac{1}{\sqrt{2\mathcal{N}}} \left[\frac{C_3^A W_+}{M} + \frac{C_4^A}{M^2} W k_0 + C_5^A \right], \\
f_{-1}^A(D_{13}) &= \frac{|\mathbf{k}|}{W} \frac{1}{\sqrt{6\mathcal{N}}} \left[\frac{C_3^A}{M} (W + M - 2k_0) - \frac{C_4^A}{M^2} W k_0 - C_5^A \right], \\
f_{0+}^{A(\lambda)}(D_{13}) &= \frac{|\mathbf{k}|}{W} \frac{1}{\sqrt{3\mathcal{N}}} \frac{1}{C_\lambda} \left[\left(\frac{C_3^A}{M} + \frac{C_4^A}{M^2} W \right) (|\mathbf{k}| \epsilon_\lambda^0 - k_0 \epsilon_\lambda^z) - C_5^A \epsilon^z + \frac{C_6^A}{M^2} |\mathbf{k}| (|\mathbf{k}| \epsilon_\lambda^0 - k_0 \epsilon_\lambda^z) \right]
\end{aligned} \tag{23}$$

where

$$\mathcal{N} = \frac{\sqrt{M^2 + \mathbf{k}^2} + M}{W}. \tag{24}$$

The coupling factors \mathcal{C}_i^V ($i = 3-5$), represent either the CC vector form factors (C_i^V), the electromagnetic form factors (C_i^N , $N = p, n$) or the NC form factors (\tilde{C}_i^N , $N = p, n$) for the resonances with spin 3/2. Similarly, \mathcal{C}_i^A , $i = 3-6$, represent either the CC axial-vector form factors (C_i^A) or NC form factors (\tilde{C}_i^A).

2. Resonance with spin 1/2

In the first and second resonance regions, there are two resonances with spin 1/2: the $P_{11}(1440)$ resonance, which has positive parity, and the $S_{11}(1535)$ resonance, which has negative parity. Their corresponding interactions are defined as follows:

$$\begin{aligned}
\Gamma_{1/2}^\rho(P_{11}) &= [\mathcal{V}_{1/2}^\rho - \mathcal{A}_{1/2}^\rho] \\
\Gamma_{1/2}^{\alpha\rho}(S_{11}) &= [\mathcal{V}_{1/2}^{\alpha\rho} - \mathcal{A}_{1/2}^{\alpha\rho}] \gamma^5
\end{aligned} \tag{25}$$

where the vector ($\mathcal{V}_{1/2}^{\alpha\rho}$) and axial-vector ($\mathcal{A}_{1/2}^{\alpha\rho}$) components are given by:

$$\begin{aligned}
\mathcal{V}_{1/2}^\rho &= \frac{\mathcal{F}_1^V}{2M^2} (k q^\rho - k^2 \gamma^\rho) + \frac{\mathcal{F}_2^V}{2M} (i \sigma^{\rho\alpha} k_\alpha), \\
\mathcal{A}_{1/2}^\rho &= \mathcal{F}_A \gamma^\rho \gamma^5 + \frac{\mathcal{F}_P}{M} k^\rho \gamma^5.
\end{aligned} \tag{26}$$

The vector and axial-vector helicity amplitudes for the P_{11} and S_{11} resonances can be derived from Eqs. 16 and 26. Here, we present the explicit forms of these ampli-

tudes for P_{11} resonance:

$$\begin{aligned} f_{-1}^V(P_{11}) &= \frac{|\mathbf{k}|}{\sqrt{W(E_k + M)}} \left[\mathcal{F}_1^V - \frac{\mathcal{F}_2^V}{W_+^2} k^2 \right] \\ f_{0+}^{V(\lambda)}(P_{11}) &= -\frac{1}{C_\lambda} \frac{|\mathbf{k}|}{\sqrt{2W(E_k + M)}} (|\mathbf{k}| \epsilon_\lambda^0 - k_0 \epsilon_\lambda^3) \\ &\quad \frac{1}{W_+} [\mathcal{F}_1^V - \mathcal{F}_2^V] \end{aligned} \quad (27)$$

$$\begin{aligned} f_{-1}^A(P_{11}) &= -\mathcal{F}_A \sqrt{\frac{E_k + M}{W}} \\ f_{0+}^{A(\lambda)}(P_{11}) &= \frac{1}{C_\lambda} \frac{1}{\sqrt{2W(E_k + M)}} \left[\mathcal{F}_A [(|\mathbf{k}| \epsilon_\lambda^0 - k_0 \epsilon_\lambda^3) \right. \\ &\quad \left. + \epsilon_\lambda^3 W_+] + \mathcal{F}_P \frac{|\mathbf{k}|}{M} (|\mathbf{k}| \epsilon_\lambda^0 - k_0 \epsilon_\lambda^3) \right] \end{aligned} \quad (28)$$

and for S_{11} resonance:

$$\begin{aligned} f_{-1}^V(S_{11}) &= \sqrt{\frac{(E_k + M)}{W}} \left[\frac{\mathcal{F}_1^V}{W_+^2} k^2 - \frac{\mathcal{F}_2^V}{W_+} W_- \right] \\ f_{0+}^{V(\lambda)}(S_{11}) &= \frac{1}{C_\lambda^V} \sqrt{\frac{E_k + M}{2W}} (|\mathbf{k}| \epsilon_\lambda^0 - k_0 \epsilon_\lambda^3) \\ &\quad \left[-\frac{\mathcal{F}_1^V W_-}{W_+^2} + \frac{\mathcal{F}_2^V}{W_+} \right] \end{aligned} \quad (29)$$

$$\begin{aligned} f_{-1}^A(S_{11}) &= -\mathcal{F}_A \frac{|\mathbf{k}|}{\sqrt{W(E_k + M)}} \\ f_{0+}^{A(\lambda)}(S_{11}) &= -\frac{1}{C_\lambda} \sqrt{\frac{E_k + M}{3W}} \left[\mathcal{F}_A (\epsilon_\lambda^0 W_+) \right. \\ &\quad \left. + \frac{\mathcal{F}_P}{M} (|\mathbf{k}| \epsilon_\lambda^0 - k_0 \epsilon_\lambda^3) \right] \end{aligned} \quad (30)$$

where \mathcal{F}_i^V ($i = 1, 2$), represent either the CC vector form factors (F_i^V), the electromagnetic form factors (F_i^N , $N = p, n$) or the NC form factors (\tilde{F}_i^N , $N = p, n$) for the resonances with spin 1/2. Similarly, \mathcal{F}_A and \mathcal{F}_P represent for CC (NC) axial-vector form factors F_A, F_P (F_A^N, F_P^N).

The vector form factors C_i^V and C_i^{VN} (F_i^V and F_i^{VN}) can be related to the electromagnetic form factors $C_i^{p,n}$ ($F_i^{p,n}$) as is presented in Table II.

3. Form factor parametrisation

The Meson Dominance (MD) model, which aligns with Quantum Chromodynamics (QCD) calculations, effectively describes the nucleon form factor in both perturbative and non-perturbative regimes as highlighted in [13]. This model is particularly adept at addressing the hadron-quark transition region. In this work, we

use a parametrization suggested by G. Vereshkov and N. Volchanskiy in Ref. [15].

$$C_\alpha^{(V,A)}(k^2) = \frac{C_\alpha^{(p)}(0)}{L_\alpha(k^2)} \sum_{k=1}^K \frac{a_{\alpha k}^{(V,A)} m_k^2}{m_k^2 - k^2}, \quad (\alpha = 3 - 5) \quad (31)$$

$$g_\beta^{(V,A)}(k^2) = \frac{g_\beta^{(p)}(0)}{L_\beta(k^2)} \sum_{k=1}^K \frac{b_{\beta k}^{(V,A)} m_k^2}{m_k^2 - k^2}, \quad (\beta = 1 - 2) \quad (32)$$

Here, $m_k^2 = m_{(\rho)k}^2$ represents the ρ -meson mass for the Δ ($P_{33}(1232)$) resonance, while $m_k^2 = (m_{(\omega)k}^2 + m_{(\rho)k}^2)/2$ pertains to the resonances in the second region, such as $P_{11}(1440)$, $D_{13}(1520)$, and $S_{11}(1535)$. The values for $m_{(\rho)k}$ and $m_{(\omega)k}$ are listed in Table I.

The parameters $a^{(V,A)}_{\alpha k}$ and $b^{(V,A)}_{\beta k}$, which represent the coupling constant ratios of vector and axial-vector mesons to nucleons, are not free parameters. Instead, they are constrained by the linear superconvergence relations as expressed in Eq. 15:

For $\alpha = 3$:

$$\begin{aligned} \sum_{k=1}^K a_{3k} &= 1, & \sum_{k=1}^K a_{3k} m_k^2 &= 0, \\ \sum_{k=1}^K a_{3k} m_k^4 &= 0. \end{aligned} \quad (33)$$

For $\alpha = 4, 5$:

$$\begin{aligned} \sum_{k=1}^K a_{\alpha k} &= 1, & \sum_{k=1}^K a_{\alpha k} m_k^2 &= 0, \\ \sum_{k=1}^K a_{\alpha k} m_k^4 &= 0, & \sum_{k=1}^K a_{\alpha k} m_k^6 &= 0. \end{aligned} \quad (34)$$

For $\beta = 1$:

$$\begin{aligned} \sum_{k=1}^K b_{1k} &= 1, & \sum_{k=1}^K b_{1k} m_k^2 &= 0, \\ \sum_{k=1}^K b_{1k} m_k^4 &= 0. \end{aligned} \quad (35)$$

For $\beta = 2$:

$$\begin{aligned} \sum_{k=1}^K b_{2k} &= 1, & \sum_{k=1}^K b_{2k} m_k^2 &= 0, \\ \sum_{k=1}^K b_{2k} m_k^4 &= 0, & \sum_{k=1}^K b_{2k} m_k^6 &= 0. \end{aligned} \quad (36)$$

The logarithmic renormalisation $L_{\alpha,\beta}^{(V,A)}(k^2)$ is necessary to satisfy quark-hadron duality:

$$L_{\alpha(\beta)}^{(A,V)}(k^2) = 1 + k_{\alpha(\beta)}^{(A,V)} \ln^{\alpha(\beta)} \left(1 - \frac{k^2}{\Lambda_{QCD}^2} \right) \quad (37)$$

TABLE II. Isospin relation for vector form factors where $s_W = (\frac{1}{2} - 2 \sin^2 \theta_W)$. Note that in the case of an isospin $1/2 \rightarrow 3/2$ transition, the form factors are equal for proton and neutron which is indicated by the index N (instead of p or n).

Channels	\mathcal{F}_i^V for $I = 1/2$	\mathcal{C}_i^V for $I = 1/2$	\mathcal{F}_i^V for $I = 3/2$	\mathcal{C}_i^V for $I = 3/2$
$e^- p \rightarrow e^- R^+$	F_i^p	C_i^p	F_i^N	C_i^N
$e^- p \rightarrow e^- R^0$	F_i^n	C_i^n	F_i^N	C_i^N
$\nu p \rightarrow l^- R^{++}$	—	—	$F_i^V = -F_i^N$	$C_i^V = -C_i^N$
$\nu n \rightarrow l^- R^+$	$F_i^V = F_i^p - F_i^n$	$C_i^V = C_i^p - C_i^n$	$F_i^V = -F_i^N$	$C_i^V = -C_i^N$
$\nu p \rightarrow \nu R^+$	$\tilde{F}_i^p = s_W F_i^p - \frac{1}{2} F_i^n - \frac{1}{2} F_i^s$	$\tilde{C}_i^p = s_W C_i^p - \frac{1}{2} C_i^n - \frac{1}{2} C_i^s$	$\tilde{F}_i^N = s_W F_i^N$	$\tilde{C}_i^N = s_W C_i^N$
$\nu p \rightarrow \nu R^0$	$\tilde{F}_i^p = s_W F_i^p - \frac{1}{2} F_i^n - \frac{1}{2} F_i^s$	$\tilde{C}_i^p = s_W C_i^p - \frac{1}{2} C_i^n - \frac{1}{2} C_i^s$	$\tilde{F}_i^N = s_W F_i^N$	$\tilde{C}_i^N = s_W C_i^N$

where $n_1 = n_3 \simeq 3$, $n_1 > n_2$ and $n_5 > n_3 > n_4$. This parametrisation provides a robust framework for analyzing the nucleon form factors, ensuring consistency with both theoretical predictions and experimental observations. The linear superconvergence relations play a crucial role in constraining the parameters, thereby enhancing the predictive power and reliability of the MD model in various resonance regions.

B. The Third resonance regions

The third resonance region is characterised by overlapping structures of multiple resonances, each contributing less significantly to the hadronic tensor compared to those in the earlier regions. Additionally, this region includes several resonances with spins greater than $3/2$, which are inherently more complex to describe due to the increased number of degrees of freedom.

To avoid introducing an excessive number of parameters that would complicate the analysis of these overlapping resonances, I employ the quark harmonic oscillator model [3] to calculate the production amplitudes as described in Eq. 16. This approach simplifies the problem by reducing the complexity associated with higher-spin resonances.

In fact, these amplitudes have already been calculated in previous works [2, 10], where a simple dipole form factor was used for each resonance. The hadronic current for each resonance in this region is related to a dipole form factor, parameterised by two adjustable quantities, $F_V(0)$ and M_V :

$$F_V(k^2) = F_V(0) \left(1 - \frac{k^2}{M_V^2}\right)^{-2} \left(1 - \frac{k^2}{M^2}\right)^{n/2} \quad (38)$$

Here, $F_V(k^2)$ represents the form factor as a function of the momentum transfer squared, k^2 . The parameter $F_V(0)$ correspond to the form factor's value at zero momentum transfer. The factor $(1 - \frac{k^2}{M^2})^{n/2}$ introduces

additional flexibility in the form factor to account for the effects of higher resonances where n represents the number of oscillator excitations in the quark oscillator model.

By adopting this approach, the model remains manageable while still capturing the essential physics of the third resonance region. The use of a dipole form factor with adjustable parameters allows for a more practical and streamlined analysis, facilitating the study of this complex region without sacrificing accuracy.

IV. ANALYSIS OF EXCLUSIVE SPP DATA

Accurate determination of vector and axial-vector transition form factors, as well as non-resonant nucleon-pion production amplitudes, is essential for providing reliable predictions of SPP channels. These form factors involve several adjustable parameters, which can only be accurately defined through the use of experimental data.

In this section, we conduct a comprehensive analysis of all available exclusive SPP data on proton and neutron targets. This joint analysis aims to determine the Q^2 dependence of all form factors described in the previous section, providing a detailed understanding of the underlying interaction dynamics. The analysis incorporates a wide range of data sources to ensure robust and accurate form factor determinations, considering various experimental conditions and measurements.

The vector form factors in weak interactions are closely linked to the electromagnetic form factors. As a result, electron and photon scattering data on nucleon targets are invaluable for determining the vector form factors. Conversely, pion scattering data are essential for fitting the axial-vector form factors. By combining electron, photon, pion, and neutrino scattering data, we can achieve a comprehensive and precise extraction of both vector and axial-vector form factors. This integrated approach ensures coverage of the entire kinematic range relevant for Single Pion Production (SPP) processes. A list of resonances used in the MK model is given in Table III.

TABLE III. Nucleon-resonances, Resonance's mass (M_R), width (Γ_0) and Branching ratio (χ_E) from PDG [9]. Resonance's signs (σ^D) and phases are the results of the fit.

Resonance	M_R [MeV]	Γ_0 [MeV]	χ_E	σ^D	phase
$P_{33}(1232)$	1236	130	0.994	+	0.55
$P_{11}(1440)$	1410	423	0.65	+	0.0
$D_{13}(1520)$	1519	120	0.60	+	1.68
$S_{11}(1535)$	1545	175	0.45	-	1.60
$P_{33}(1600)$	1.64	200	0.16	+	1.98
$S_{31}(1620)$	1610	130	0.3	+	—
$F_{15}(1680)$	1685	120	0.65	-	—
$D_{33}(1700)$	1710	300	0.15	+	—
$P_{11}(1710)$	1710	140	0.11	-	—
$P_{13}(1720)$	1720	250	0.11	+	—
$F_{35}(1905)$	1880	330	0.12	-	—
$P_{31}(1910)$	1900	300	0.22	+	—
$P_{33}(1920)$	1920	300	0.12	-	—
$F_{37}(1950)$	1930	285	0.40	+	—

A. Photo-Nucleon and Electro-Nucleon Single Pion Productions

Electron and photon scattering data are crucial for this analysis as they allow for probing the vector current operators using monochromatic incident beams across a wide range of kinematic regions. Given the limitations of theoretical predictions in accurately capturing the Q^2 -dependence of form factors, particularly in the transition region, this experimental data is crucial for guiding the selection of optimal functions for various vector form factors, which are then applied to axial-vector form factors. The interactions of electrons and photons with protons are described by the following reactions:

$$e + p \rightarrow ep \pi^0, \quad e + p \rightarrow en \pi^+ \quad (39)$$

$$\gamma + p \rightarrow p \pi^0, \quad \gamma + p \rightarrow n \pi^+ \quad (40)$$

Similarly, the interactions of electrons and photons with neutrons are:

$$e + n \rightarrow en \pi^0, \quad e + n \rightarrow ep \pi^-$$

$$\gamma + n \rightarrow n \pi^0, \quad \gamma + n \rightarrow p \pi^-. \quad (41)$$

In previous work presented in Ref. [6], the model for electron-proton interactions and the electromagnetic MD form factors were tested for their ability to describe excited protons within the transition region. In that study, the MD form factors were fitted to all available electron-proton scattering data in the two channels described by Eq. 39. The results demonstrated that the model could predict the data smoothly and accurately across these kinematic ranges.

In the current study, we adopt a similar analysis methodology but extend it by including photo-proton

TABLE IV. Electromagnetic data used in the analysis, spanning a wide kinematic range across multiple channels in electron and photon scattering measurements. The photon scattering data is sourced from various measurements conducted with different energy beams.

Channel	E_e GeV	Q^2 (GeV/c) ²	W GeV
$ep \rightarrow ep \pi^0$	1.046	0.16 - 0.32	1.1 - 1.34
$ep \rightarrow en \pi^+$	1.046	0.16 - 0.32	1.1 - 1.34
$ep \rightarrow en \pi^+$	1.515	0.30 - 0.60	1.11 - 1.57
$ep \rightarrow ep \pi^0$	1.645	0.40 - 0.90	1.1 - 1.68
$ep \rightarrow ep \pi^0$	2.445	0.65 - 1.80	1.1 - 1.68
$ep \rightarrow en \pi^+$	5.499	1.80 - 4.00	1.62 - 2.01
$ep \rightarrow en \pi^+$	5.754	1.72 - 4.16	1.15 - 1.67
$ep \rightarrow ep \pi^0$	5.754	3.00 - 6.00	1.11 - 1.39
$en \rightarrow ep \pi^-$	2.039	0.4 - 1.0	1.1 - 1.8
$\gamma n \rightarrow \gamma p \pi^-$	-	0.00	1.1 - 2.01
$\gamma p \rightarrow \gamma n \pi^+$	-	0.00	1.1 - 2.01

scattering data in Eq. 40. This inclusion is particularly important for addressing the form factors at very low Q^2 , a region that is less accessible through electron scattering alone. Photo-nucleon interactions provide complementary information that helps fill in these gaps, ensuring a more comprehensive understanding of the form factors across all relevant kinematic regions.

This study expands the investigation by incorporating data on surface plasmon polaritons (SPPs) induced by electrons and photons on neutron targets, as shown in Eq. 41. The recent analysis of π^- production with an electron beam has made this analysis possible for the first time. This advancement is crucial for determining the form factors of excited neutrons, a subject that has been less studied compared to protons.

The form factors obtained from interactions involving excited protons and neutrons are anticipated to be identical for isospin 3/2 resonances due to isospin symmetry considerations, as discussed by Lalakulich et al. [8]. However, for isospin 1/2 resonances, differences can emerge, reflecting the distinct internal dynamics of these states. Understanding these discrepancies is essential for a comprehensive understanding of nucleon resonance behavior.

B. Pion-Nucleon and Neutrino-Nucleon Single Pion Productions

Neutrino interactions with weak current can provide information for both vector and axial-vector currents. The SPP neutrino interactions consist of CC and NC channels for neutrino and anti-neutrino beams. The

charged current SPP channels are:

$$\begin{aligned} \nu_l + p &\rightarrow l^- p \pi^+ , & \bar{\nu}_l + n &\rightarrow l^+ n \pi^- \\ \nu_l + n &\rightarrow l^- n \pi^+ , & \bar{\nu}_l + p &\rightarrow l^+ p \pi^- \\ \nu_l + n &\rightarrow l^- p \pi^0 , & \bar{\nu}_l + p &\rightarrow l^+ n \pi^0 \end{aligned} \quad (42)$$

and the neutral current SPP channels are:

$$\begin{aligned} \nu_l + p &\rightarrow \nu_l p \pi^0 , & \bar{\nu}_l + p &\rightarrow \bar{\nu}_l p \pi^0 \\ \nu_l + p &\rightarrow \nu_l n \pi^+ , & \bar{\nu}_l + p &\rightarrow \bar{\nu}_l n \pi^+ \\ \nu_l + n &\rightarrow \nu_l n \pi^0 , & \bar{\nu}_l + n &\rightarrow \bar{\nu}_l n \pi^0 \\ \nu_l + n &\rightarrow \nu_l p \pi^- , & \bar{\nu}_l + n &\rightarrow \bar{\nu}_l p \pi^- \end{aligned} \quad (43)$$

Experimental knowledge of the neutrino-nucleon cross section for single pion production in the GeV neutrino energy range, which is crucial for current and planned neutrino oscillation experiments, remains limited. Most of the existing data originate from low-statistics bubble chamber experiments conducted with hydrogen or deuterium targets and involve muon (anti-)neutrino beams.

Unlike electron scattering experiments, where full kinematic measurements are typically available, neutrino data are generally reported as integrated cross sections or one-dimensional differential cross sections. The only data available on hydrogen targets are from CC neutrino and anti-neutrino channels measured by the BEBC experiment, which utilised very broad neutrino and anti-neutrino beams. Consequently, the most relevant weak interaction data for this study is the Q^2 -differential cross section obtained from the BEBC experiment.

There are more data on deuterium targets from the ANL and BNL bubble chamber experiments with neutrino beams in the few GeV range, which are more relevant for this study. In fact, all single pion production (SPP) models have used the ANL and BNL data to fit the axial form factor, assuming that nuclear effects on deuterium are negligible. However, recent measurements with an electron beam [14] indicate that the cross sections for hydrogen and deuterium differ by approximately 15%.

As a result, I am not using the direct cross-section measurements on deuterium targets, as the nuclear effects are not negligible. Nevertheless, I assume that the ratio of the cross-section data across different channels will effectively cancel out the nuclear effects. Consequently, the already limited neutrino data will become even more restricted.

Fortunately, pion scattering data on hydrogen can provide additional information for determining the axial form factor. The weak interaction, which includes both vector and axial vector currents, only has contributions from the axial vector current at very low $Q^2 \sim 0$. This phenomenon is explained by the conserved vector current (CVC) relation. In this region, the axial vector current is connected to elastic pion-nucleon interactions via the partially conserved axial current (PCAC) relation:

$$\begin{aligned} \left. \frac{d\sigma}{dW dQ^2}(\nu_\mu p \rightarrow \mu^- p \pi^+) \right|_{Q^2=0} &= \sigma(\pi^+ p \rightarrow \pi^+ p) \\ \left. \frac{d\sigma}{dW dQ^2}(\bar{\nu}_\mu p \rightarrow \mu^+ p \pi^-) \right|_{Q^2=0} &= \sigma(\pi^- p \rightarrow \pi^- p) \end{aligned} \quad (44)$$

(45)

Therefore, the axial form factors are fitted to the pion scattering data at very low Q^2 . The Q^2 -dependence of the axial form factors can only be determined using neutrino-nucleon single pion production (SPP) data, which is very scarce.

The model includes 88 parameters to parametrise all the transition form factors for resonance production and non-resonant background. These parameters are fit to the experimental data by using the Minuit2 minimiser and the best fit result, with a reduced $\chi^2 = 3.05$, are discussed below:

V. CONCLUSION

The Single Pion Production (SPP) model presented in this work is meticulously designed to enhance our understanding and interpretation of neutrino measurements:

- **Comprehensive Coverage:** The model encompasses all SPP channels and is applicable across the entire kinematic range relevant to the energy spans of all neutrino experiments.
- **NC Weak Interaction:** By employing a unified model of electromagnetic and weak interactions along with isospin symmetry, the model delivers precise predictions for NC neutrino interactions, even in the absence of extensive data. This capability is particularly crucial for water Cherenkov detectors such as T2K and Hyper-K, where neutral current π^0 production constitutes a significant background.
- **Addressing Low Q^2 :** The model effectively addresses the low Q^2 region, where discrepancies with data currently exist. This is achieved through the use of photon scattering data and the Conserved Vector Current (CVC) hypothesis for the vector current, as well as pion scattering data and Partially Conserved Axial Current (PCAC) for the axial current.
- **Addressing High Q^2 :** Neutrino-nucleon-resonance vertices are parameterized with phenomenological form factors that possess analytic properties and adhere to the unitarity condition. These form factors are asymptotically consistent with QCD calculations, ensuring the model's validity at high Q^2 .

- **Addressing High W :** The model extends its validity to high W by utilizing Regge phenomenology, replacing t-channel Feynman propagators in non-resonant interactions with the corresponding Regge trajectories.
- **Integration with Event Generators:** The model is designed for seamless integration into nuclear theory frameworks and neutrino event generators employed by neutrino experiments, ensuring accurate and consistent predictions.
- **Systematic Uncertainty Control:** The calculations are conducted with stringent control over systematic uncertainties stemming from experimental errors, model dependencies, parameterization choices, and extrapolation to higher energies. This rigorous approach is crucial for the reliability and precision of neutrino measurements.

By addressing these key areas, the SPP model provides a robust framework for enhancing the accuracy and reliability of neutrino and anti-neutrino interaction studies, paving the way for more precise and insightful experimental results and CP discovery.

Appendix A: Helicity amplitudes for the resonant interactions

The helicity amplitudes of the vector and axial-vector currents are given in Table VI and Table VII, where $f^{V,A}(R)$ is the production amplitudes and $D(R)$ is the decay amplitude:

$$\mathcal{D}^j(R) = \langle N\pi, \lambda_2 | R \lambda_R \rangle = \sigma^D C_{N\pi}^j \sqrt{\chi_E \kappa} C_{N\pi}^I f_{BW} \quad (\text{A1})$$

where $f_{BW}(R)$ is the Breit-Wigner amplitude:

$$f_{BW}(R) = \sqrt{\frac{\Gamma_R}{2\pi}} \left(\frac{1}{W - M_R + i\Gamma_R/2} \right) \quad (\text{A2})$$

where

$$\Gamma_R = \Gamma_0 (|\mathbf{q}(W)|/|\mathbf{q}(M_R)|)^{2l+1}, \quad (\text{A3})$$

and

$$\kappa = \left(2\pi^2 \frac{W^2}{M^2} \cdot \frac{2}{2j+1} \frac{1}{|\mathbf{q}|} \right)^{\frac{1}{2}}, \quad (\text{A4})$$

Γ_0 , M_R , σ^D and χ_E are given in Table III and $C_{N\pi}^I$ are the isospin Clebsch-Gordan coefficients given in Table V. The explicit form of the $d_{\lambda,\mu}^j(\theta)$ functions for $j = l + \frac{1}{2}$

TABLE V. Isospin coefficients

Channels	$C_{N\pi}^{3/2}$	$C_{N\pi}^{1/2}$
$ep \rightarrow ep\pi^0$	$\sqrt{\frac{2}{3}}$	$-\sqrt{\frac{1}{3}}$
$ep \rightarrow en\pi^+$	$-\sqrt{\frac{1}{3}}$	$-\sqrt{\frac{2}{3}}$

are:

$$\begin{aligned} d_{\frac{1}{2}\frac{1}{2}}^j &= (l+1)^{-1} \cos \frac{\theta}{2} (P'_{l+1} - P'_l) \\ d_{-\frac{1}{2}\frac{1}{2}}^j &= (l+1)^{-1} \sin \frac{\theta}{2} (P'_{l+1} + P'_l) \\ d_{\frac{1}{2}\frac{3}{2}}^j &= (l+1)^{-1} \sin \frac{\theta}{2} \left(\sqrt{\frac{l}{l+2}} P'_{l+1} + \sqrt{\frac{l+2}{l}} P'_l \right) \\ d_{-\frac{1}{2}\frac{3}{2}}^j &= (l+1)^{-1} \cos \frac{\theta}{2} \left(-\sqrt{\frac{l}{l+2}} P'_{l+1} + \sqrt{\frac{l+2}{l}} P'_l \right) \end{aligned}$$

where P_l are Legendre polynomials and $P'_l = dP_l/d\cos\theta$.

-
- [1] Cyril Adamuscin, Anna-Zuzana Dubnickova, Stanislav Dubnicka, Roman Pekarik, and Peter Weisenpacher. *Eur. Phys. J. C*, 28:115–118, 2003. doi:10.1140/epjc/s2003-01143-3.
 - [2] Ch. Berger and L. M. Sehgal. Lepton mass effects in single pion production by neutrinos. *Phys. Rev. D*, 76: 113004, 2007. doi:10.1103/PhysRevD.76.113004.
 - [3] R. P. Feynman, M. Kislinger, and F. Ravndal. Current matrix elements from a relativistic quark model. *Phys. Rev. D*, 3:2706–2732, 1971. doi: 10.1103/PhysRevD.3.2706.
 - [4] Murray Gell-Mann and Fredrik Zachariasen. Form-factors and vector mesons. *Phys. Rev.*, 124:953–964, 1961. doi:10.1103/PhysRev.124.953.
 - [5] M. Kabirnezhad. Single pion production in electron-nucleon interactions. *Phys. Rev. D*, 102(5):053009, 2020. doi:10.1103/PhysRevD.102.053009.
 - [6] M. Kabirnezhad. Single-pion production in electron-proton interactions. *Phys. Rev. C*, 107(2):025502, 2023. doi:10.1103/PhysRevC.107.025502.
 - [7] Monireh Kabirnezhad. Single pion production in neutrino-nucleon Interactions. *Phys. Rev. D*, 97(1): 013002, 2018. doi:10.1103/PhysRevD.97.013002.
 - [8] Olga Lalakulich, Emmanuel A. Paschos, and Giorgi Piranishvili. Resonance production by neutrinos: The Second resonance region. *Phys. Rev. D*, 74:014009, 2006. doi:10.1103/PhysRevD.74.014009.
 - [9] S. Navas et al. Review of particle physics. *Phys. Rev. D*, 110(3):030001, 2024. doi:10.1103/PhysRevD.110.030001.
 - [10] Dieter Rein and Lalit M. Sehgal. Neutrino Excitation of Baryon Resonances and Single Pion Production. *Annals Phys.*, 133:79–153, 1981. doi:10.1016/0003-

Appendix B: Helicity amplitudes for the non-resonant interactions

TABLE VIII. Vector helicity amplitudes of non-resonant interaction.

λ_2	λ_1	$\tilde{F}_{\lambda_2\lambda_1}^{e_L}(\theta, \phi)$	$\tilde{F}_{\lambda_2\lambda_1}^{e_R}(\theta, \phi)$
$\frac{1}{2}$	$\frac{1}{2}$	$\frac{1}{\sqrt{2}}e^{-2i\phi}\sin\theta\cos\frac{\theta}{2}(\mathcal{F}_3 + \mathcal{F}_4)$	$-\sqrt{2}\left[\sin\frac{\theta}{2}(\mathcal{F}_1 + \mathcal{F}_2) + \frac{1}{2}\sin\theta\cos\frac{\theta}{2}(\mathcal{F}_3 + \mathcal{F}_4)\right]$
$-\frac{1}{2}$	$\frac{1}{2}$	$-\frac{1}{\sqrt{2}}e^{-i\phi}\sin\theta\sin\frac{\theta}{2}(\mathcal{F}_3 - \mathcal{F}_4)$	$-\sqrt{2}e^{i\phi}\left[\cos\frac{\theta}{2}(\mathcal{F}_1 - \mathcal{F}_2) - \frac{1}{2}\sin\theta\sin\frac{\theta}{2}(\mathcal{F}_3 - \mathcal{F}_4)\right]$
$\frac{1}{2}$	$-\frac{1}{2}$	$\sqrt{2}e^{-i\phi}\left[\cos\frac{\theta}{2}(\mathcal{F}_1 - \mathcal{F}_2) - \frac{1}{2}\sin\theta\sin\frac{\theta}{2}(\mathcal{F}_3 - \mathcal{F}_4)\right]$	$\frac{1}{\sqrt{2}}e^{i\phi}\sin\theta\sin\frac{\theta}{2}(\mathcal{F}_3 - \mathcal{F}_4)$
$-\frac{1}{2}$	$-\frac{1}{2}$	$-\sqrt{2}\left[\sin\frac{\theta}{2}(\mathcal{F}_1 + \mathcal{F}_2) + \frac{1}{2}\sin\theta\cos\frac{\theta}{2}(\mathcal{F}_3 + \mathcal{F}_4)\right]$	$\frac{1}{\sqrt{2}}e^{2i\phi}\sin\theta\cos\frac{\theta}{2}(\mathcal{F}_3 + \mathcal{F}_4)$
		$\tilde{F}_{\lambda_2\lambda_1}^{e_-}(\theta, \phi)$	$\tilde{F}_{\lambda_2\lambda_1}^{e_+}(\theta, \phi)$
$\frac{1}{2}$	$\frac{1}{2}$	$e^{-i\phi}\cos\frac{\theta}{2}\frac{1}{C_-}(k_0\epsilon_L^0 - \mathbf{k} \epsilon_L^3)(\mathcal{F}_5 + \mathcal{F}_6)$	$e^{-i\phi}\cos\frac{\theta}{2}\frac{1}{C_+}(k_0\epsilon_R^0 - \mathbf{k} \epsilon_R^3)(\mathcal{F}_5 + \mathcal{F}_6)$
$-\frac{1}{2}$	$\frac{1}{2}$	$-\sin\frac{\theta}{2}\frac{1}{C_-}(k_0\epsilon_L^0 - \mathbf{k} \epsilon_L^3)(\mathcal{F}_5 - \mathcal{F}_6)$	$-\sin\frac{\theta}{2}\frac{1}{C_+}(k_0\epsilon_R^0 - \mathbf{k} \epsilon_R^3)(\mathcal{F}_5 - \mathcal{F}_6)$
$\frac{1}{2}$	$-\frac{1}{2}$	$-\sin\frac{\theta}{2}\frac{1}{C_-}(k_0\epsilon_L^0 - \mathbf{k} \epsilon_L^3)(\mathcal{F}_5 - \mathcal{F}_6)$	$-\sin\frac{\theta}{2}\frac{1}{C_+}(k_0\epsilon_R^0 - \mathbf{k} \epsilon_R^3)(\mathcal{F}_5 - \mathcal{F}_6)$
$-\frac{1}{2}$	$-\frac{1}{2}$	$-e^{i\phi}\cos\frac{\theta}{2}\frac{1}{C_-}(k_0\epsilon_L^0 - \mathbf{k} \epsilon_L^3)(\mathcal{F}_5 + \mathcal{F}_6)$	$-e^{i\phi}\cos\frac{\theta}{2}\frac{1}{C_+}(k_0\epsilon_R^0 - \mathbf{k} \epsilon_R^3)(\mathcal{F}_5 + \mathcal{F}_6)$

- 4916(81)90242-6.
- [11] J. J. Sakurai. Theory of strong interactions. *Annals Phys.*, 11:1–48, 1960. doi:10.1016/0003-4916(60)90126-3.
- [12] Jan T. Sobczyk and Jakub Zmuda. Investigation of recent weak single-pion production data. *Phys. Rev.*, C91(4): 045501, 2015. doi:10.1103/PhysRevC.91.045501.
- [13] P. Stoler. *Phys. Rept.*, 226:103–171, 1993.
- [14] Y. Tian et al. Exclusive π^- electroproduction off the neutron in deuterium in the resonance region. *Phys. Rev. C*, 107(1):015201, 2023. doi:10.1103/PhysRevC.107.015201.
- [15] G. Vereshkov and N. Volchanskiy. *Phys. Rev. D*, 76: 073007, 2007.